CrossMark

# The Power of the Rings: The GRB 221009A Soft X-Ray Emission from Its Dust-scattering Halo

Andrea Tiengo[1,2], Fabio Pintore[3], Beatrice Vaia[1,2,4], Simone Filippi[1,5], Andrea Sacchi[1], Paolo Esposito[1,2], Michela Rigoselli[2], Sandro Mereghetti[2], Ruben Salvaterra[2], Barbara Šiljeg[6,7,8], Andrea Bracco[9], Željka Bošnjak[10], Vibor Jelić[8], and Sergio Campana[11]

[1] Scuola Universitaria Superiore IUSS Pavia, Piazza della Vittoria 15, I-27100 Pavia, Italy
[2] Istituto Nazionale di Astrofisica, Istituto di Astrofisica Spaziale e Fisica Cosmica di Milano, via A. Corti 12, I-20133 Milano, Italy
[3] Istituto Nazionale di Astrofisica, Istituto di Astrofisica Spaziale e Fisica Cosmica di Palermo, Via U. La Malfa 153, I-90146 Palermo, Italy
[4] Department of Physics, University of Trento, Via Sommarive 14, I-38123 Povo (TN), Italy
[5] Department of Physics "A. Volta," University of Pavia, Via Bassi 6, I-27100 Pavia, Italy
[6] ASTRON, the Netherlands Institute for Radio Astronomy, Oude Hoogeveensedijk 4, 7991 PD Dwingeloo, The Netherlands
[7] Kapteyn Astronomical Institute, University of Groningen, P.O. Box 800, 9700 AV, Groningen, The Netherlands
[8] Ruđer Bošković Institute, Bijenička cesta 54, 10000 Zagreb, Croatia
[9] Laboratoire de Physique de l'Ecole Normale Supérieure, ENS, Université PSL, CNRS, Sorbonne Université, Université de Paris, F-75005 Paris, France
[10] Faculty of Electrical Engineering and Computing, University of Zagreb, Unska ul.3, 10000 Zagreb, Croatia
[11] Istituto Nazionale di Astrofisica, Osservatorio Astronomico di Brera, Via E. Bianchi 46, I-23807 Merate (LC), Italy

## Abstract

GRB 221009A is the brightest gamma-ray burst (GRB) ever detected that has occurred at low Galactic latitude. Owing to this exceptional combination, its prompt X-ray emission could be detected for weeks in the form of expanding X-ray rings produced by scattering in Galactic dust clouds. We report on the analysis of 20 rings, generated by dust at distances ranging from 0.3 to 18.6 kpc, detected during two X-ray Multi Mirror (XMM)-Newton observations performed about 2 and 5 days after the GRB. By fitting the spectra of the rings with different models for the dust composition and grain size distribution, we reconstructed the spectrum of the GRB prompt emission in the 0.7–4 keV energy range as an absorbed power law with photon index $\Gamma = 1$–1.4 and absorption in the host galaxy $N_{\mathrm{H},z} = (4.1$–$5.3) \times 10^{21}$ cm$^{-2}$. Taking into account the systematic uncertainties regarding the column density of dust contained in the clouds producing the rings, the 0.5–5 keV fluence of GRB 221009A can be constrained between $10^{-3}$ and $7 \times 10^{-3}$ erg cm$^{-2}$. Both the fluence and the photon index indicate the presence of a possible soft excess with respect to the extrapolation of the main GRB peak observed at higher energies.

*Unified Astronomy Thesaurus concepts:* Gamma-ray bursts (629); Interstellar dust (836); Interstellar dust extinction (837); Interstellar scattering (854)

## 1. Introduction

The gamma-ray burst (GRB) 221009A was first reported when its hard X-ray (>15 keV) emission triggered the Swift Neil Gehrels observatory/Burst Alert Telescope (Swift/BAT) instrument on 2022 October 9 at 14:10:17 UT (Dichiara et al. 2022), but owing to its low Galactic latitude and long duration, it was initially believed to be a new Galactic transient. However, it was soon realized that it was the afterglow of a very bright and long GRB, which had been detected with the Gamma-Ray Burst Monitor (GBM; 10 keV–25 MeV) on board Fermi about 1 hr earlier (Kennea et al. 2022; Veres et al. 2022).[12]

GRB 221009A is the brightest GRB ever observed (Burns et al. 2023): most of the X-/gamma-ray instruments were saturated (or strongly affected by dead time or pileup) during the peak of its emission. Such an exceptional brightness resulted from the combination of a high intrinsic luminosity and close distance (745 Mpc; Malesani et al. 2023). It has been estimated that the occurrence of a burst of this luminosity

within this distance might be once every 10,000 yr (Burns et al. 2023).

GRB 221009A occurred close to the direction of the Galactic plane ($b = 4°\!.32$ and $l = 52°\!.96$) and, remarkably, produced several bright X-ray scattering rings caused by interstellar dust in our Galaxy (Tiengo et al. 2022; Williams et al. 2023). Dust-scattering rings have been observed so far only in a handful of GRBs (Vaughan et al. 2004; Tiengo & Mereghetti 2006; Vaughan et al. 2006; Vianello et al. 2007; Pintore et al. 2017). Their study is useful to derive information on the dust (e.g., its distance, composition, and grain size distribution) as well as on the properties of the GRB prompt emission in the soft X-ray range, which usually cannot be observed directly.

Here we report on the dust-scattering rings of GRB 221009A as observed with the X-ray Multi Mirror (XMM)-Newton satellite. Our main objective is to estimate fluence and spectral shape of the prompt emission in the soft X-ray range (0.7–4 keV). A more complete exploitation of this exceptional data set to characterize the dust properties is deferred to forthcoming publications.

The distances of the scattering dust layers can be derived from the angular expansion rate of the rings, caused by the longer path length of the photons scattered at larger angles (Trümper & Schönfelder 1973). On the other hand, inferring the GRB properties from the observed rings is more complicated and requires some assumptions. Indeed, since the specific intensity of the scattered radiation is proportional to the product of the burst

---

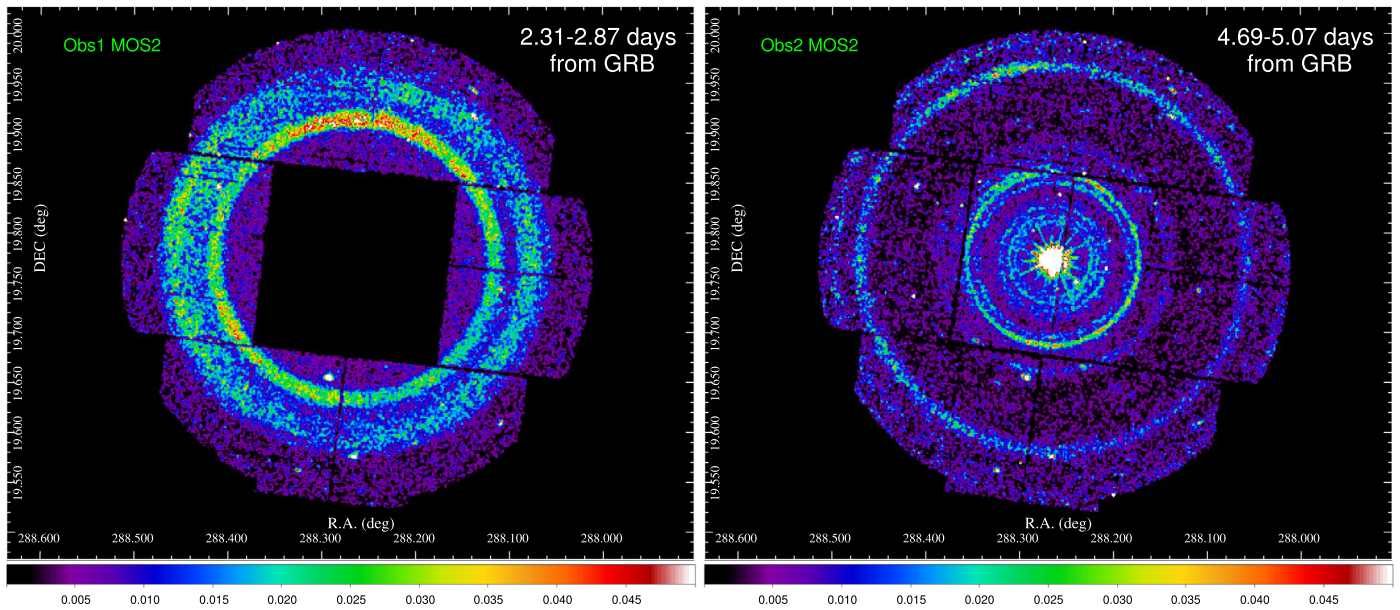[12] Swift was occulted by the Earth at the time of the GRB onset.

**Figure 1.** EPIC-MOS2 exposure-corrected 0.7–4 keV images, in units of counts s$^{-1}$ arcmin$^{-2}$, of the expanding rings from Obs1 (left panel) and Obs2 (right panel). All the images have been smoothed with a Gaussian kernel of $\sigma = 3\rlap{.}''5$.

fluence and dust optical depth, some independent information is required to break the degeneracy between these two quantities. Thanks to the high statistical quality of our X-ray observations, which allow us to measure the spectra of a large number of rings as well as their time evolution and azimuthal brightness variations, we could compare the results obtained with various methods and assumptions, thus deriving the spectrum of the GRB prompt emission in the soft X-ray range with a realistic estimate of the systematic uncertainties. In particular, we considered the cross sections corresponding to eight different models of interstellar dust grains (Mathis et al. 1977; Draine 2003; Zubko et al. 2004). We also used various studies of optical extinction in this direction: three-dimensional (3D) maps to estimate the contributions of individual dust layers (Green et al. 2019; Lallement et al. 2022) and two-dimensional (2D) maps to derive the integrated absorption along the whole line of sight (Schlafly & Finkbeiner 2011; Planck Collaboration 2014).

## 2. Observations

The first XMM-Newton observation (Obs.ID 0913991501, hereafter Obs1) started on 2022 October 11 at 21:11:10, about 2.3 days after the GRB trigger, and lasted about 50 ks. The main aim of this observation was the study of the X-ray afterglow, which was still extremely bright. Therefore, to minimize the photon pileup, the European Photon Imaging Camera (EPIC) PN (Strüder et al. 2001) and the two EPIC Metal Oxide Semiconductor (MOS; Turner et al. 2001) cameras were operated in Timing mode, with the thick optical-blocking filter. In Timing mode, full imaging capabilities are provided only by the peripheral CCDs of the MOS cameras.[13] Since the size of each MOS CCD is $11' \times 11'$, X-ray rings with radii smaller than $5\rlap{.}'5$ could not be observed, and only MOS2 could image the whole azimuthal extent of the rings. The particle background remained low and constant

throughout the whole observation, resulting in a net exposure time of 47.8 ks for the MOS2.

A second observation (Obs.ID 0913991601, hereafter Obs2), with a total duration of 62 ks, was performed on 2022 October 14. Since it was mainly devoted to the study of the rings, all the EPIC cameras were operated in full-frame mode, which provides full imaging capabilities over the whole field of view ($\sim$14$'$ radius), and the thin optical filter was used. The second part of this observation was affected by strong and variable particle background. Therefore, we limited the analysis to the longest uninterrupted time interval with quiescent background for both the PN and MOS2 cameras.[14] This resulted in a net exposure time of 29.7 ks for the PN and 33.5 ks for the MOS2.

Further XMM-Newton observations, carried out 21, 23, and 32 days after the GRB, are crucial to better characterize the properties of the dust clouds located on the most distant dust clouds, which produce X-ray rings with a slower time evolution and are therefore still bright enough and well within the EPIC field of view at such late times. However, we will not use them because, due to the faintness of the rings, they do not give a substantial contribution to the reconstruction of the GRB prompt X-ray emission, which is the main aim of the present work.

## 3. Data Analysis and Results

The data were processed using SAS 19.1.0 (Gabriel et al. 2004) and the most recent calibration files. The EPIC events were cleaned using standard filtering expressions. To maximize the signal-to-noise ratio of the rings, the analysis was restricted to the 0.7–4 keV energy band.

The MOS2 images of the two observations are shown in Figure 1. Some of the X-ray rings that were visible in the first observation (left panel) have moved (partly) outside the field of

---

[13] Six CCDs in MOS2 and only four in MOS1 because two of them were permanently damaged in the early phases of the mission.

[14] MOS1 data were also checked for consistency, but MOS1 results are not reported because the two missing CCDs did not allow us to fully cover the rings with a radius larger than $5\rlap{.}'5$.

view in the second one (right panel), but several additional rings, produced by dust clouds at larger distances, have become accessible at radii $<6'$. These images show that the surface brightness of the individual rings is not uniform (see also Appendix A), which indicates that the dust clouds responsible for the scattering are not homogeneous in the plane of the sky.

A number of point-like sources are apparent, and for the ring analysis they were removed by excluding circular regions of radius $\sim20''$. Out-of-time events were also removed following the standard procedure.[15]

### 3.1. Galactic Dust Distribution

We studied the expanding dust-scattering rings by adopting the approach of the so-called pseudodistance distribution (Tiengo & Mereghetti 2006). For each detected event we compute the quantities

$$t_i = T_i - T_0 \tag{1}$$

$$\theta_i^2 = (x_i - X_{\mathrm{GRB}})^2 + (y_i - Y_{\mathrm{GRB}})^2, \tag{2}$$

where $x_i$, $y_i$, and $T_i$ are the detector coordinates and the time of arrival of the i event; $T_0$, $X_{\mathrm{GRB}}$ and $Y_{\mathrm{GRB}}$ are the GRB start time and detector coordinates. $T_0$ is fixed at MJD=59,861.55568, when the bulk of the prompt emission of GRB 221009A was detected, and the GRB coordinates are derived by taking the central position of the afterglow in each observation. The pseudodistance is defined as

$$D_i = 2ct_i/\theta_i^2 = (19.85 t_i[\mathrm{days}])/(\theta_i^2[\mathrm{arcmin}]) \, \mathrm{kpc}. \tag{3}$$

For background events, this quantity is not a real distance. Instead, photons from an expanding ring have values of $D_i$ that cluster around the distance of the scattering dust layer.

The histograms of pseudodistances obtained in the two observations (Figure 2) clearly show a number of peaks that indicate the presence of many dust-scattering layers at different distances. We fit separately the histogram of each instrument with the sum of a power law (to account for the background) and a series of Lorentzian functions (9 for Obs1 and 19 for Obs2). The best-fit values obtained for the peak centroids and widths[16] are reported in Table 1, together with the angular radii ($\theta_1$ and $\theta_2$) of the rings at the beginning and at the end of each observation, derived from Equation (3).

In total, we identified 20 dust layers, with the most prominent ones clustered at distances in the range 400–750 pc. We also located a group of dust layers between 2 and 5 kpc and another one between 10 and 20 kpc.

### 3.2. Spectral Analysis and Results

The ring spectra were extracted by fitting Lorentzian functions to the peaks in the energy-resolved pseudodistance distributions, assuming a power-law model for the background
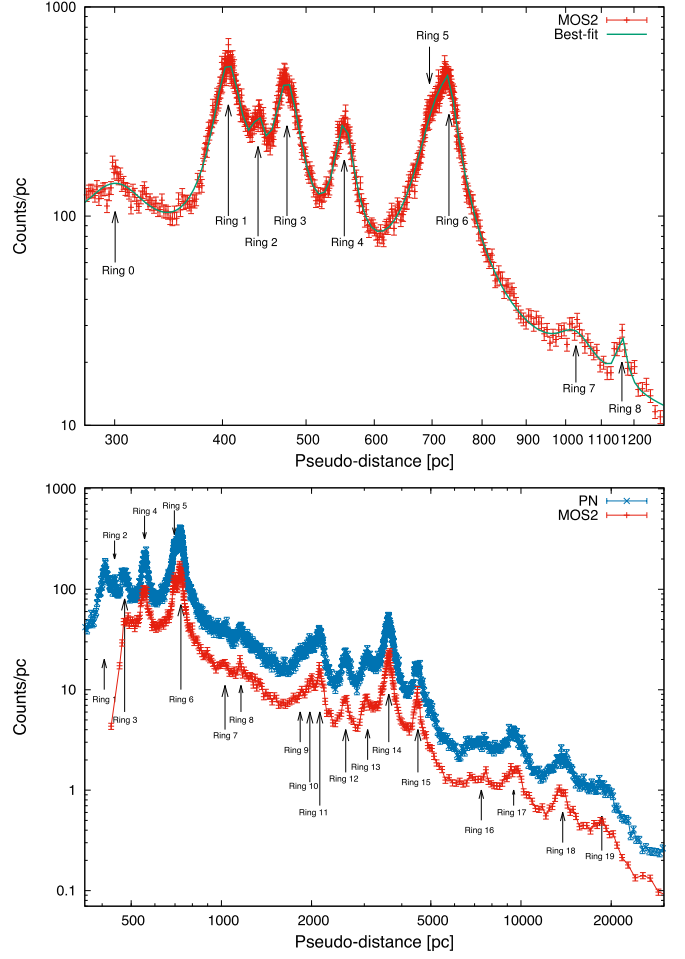
---

[15] https://www.cosmos.esa.int/web/xmm-newton/sas-thread-epic-oot

[16] The width of a peak in the pseudodistance distribution depends on the GRB duration (negligible in this case), the instrumental point-spread function (PSF; $\sim20''$ half-energy width), and the intrinsic thickness of the dust layer (Vianello et al. 2007).



**Figure 2.** Pseudodistance distributions in the 0.7–4 keV energy band for the two XMM-Newton observations (Obs1: top; Obs2: bottom). Arrows indicate the number of the rings as reported in Table 1. MOS2 data are in red and PN in blue. The green line of the top panel indicates the best-fit model with a power law plus 9 Lorentzian functions.

contribution (as explained in Tiengo & Mereghetti 2006 and Pintore et al. 2017). The Lorentzian centroids and widths were kept fixed to the values obtained for each observation and instrument in the whole 0.7–4 keV energy band (Figure 2). Their normalizations were instead derived in suitable energy intervals, chosen to have at least 100 net counts in each peak. For each spectrum, response matrices were produced with the SAS tasks rmfgen and arfgen for the annular regions covered by each ring during the observation. The matrices are not corrected for the instrumental PSF since the integration of the Lorentzian functions from which the spectral bins are generated already comprises all the background-subtracted counts in the ring.

The spectrum $F(E)$ of a ring produced by the single-scattering of GRB photons with energy $E$ in a geometrically thin dust cloud in our Galaxy, as observed to expand from $\theta_1$ to $\theta_2$, can be written as

$$F(E) = \frac{f(E)}{T_{\mathrm{exp}}} \Delta N_{\mathrm{H}} \sigma_{\theta_{1,2}}(E), \tag{4}$$

where $f(E)$ is the GRB specific fluence, $T_{\mathrm{exp}}$ is the observation duration, $\Delta N_{\mathrm{H}}$ is the equivalent hydrogen column density of dust in the cloud, and $\sigma_{\theta_{1,2}}(E)$ is the scattering cross section

**Table 1**
Ring Distances, Widths (FWHM of the Lorentzian Peaks in Figure 2), and Expected Radii in the Two XMM-Newton Observations

| Ring | Distance (pc) | Width (pc) | $\theta_1 - \theta_2$ in Obs1; Obs2 (arcmin) |
|---|---|---|---|
| 0 | $300 \pm 2$ | $62 \pm 10$ | (12.41–13.81); (17.66–18.37) |
| 1 | $406.3 \pm 0.2$ | $26.9 \pm 0.7$ | 10.67–11.86; (15.17–15.79) |
| 2 | $439.8 \pm 0.5$ | $14.6 \pm 1.9$ | 10.25–11.40; (14.59–15.17) |
| 3 | $475.2 \pm 0.3$ | $30.9 \pm 0.9$ | 9.86–10.97; (14.03–14.60) |
| 4 | $553.6 \pm 0.3$ | $27.7 \pm 1.0$ | 9.14–10.16; (13.00–13.52) |
| 5 | $695.4 \pm 1.2$ | $23.1 \pm 3.7$ | 8.15–9.07; 11.60–12.07 |
| 6 | $728.6 \pm 1.1$ | $42.7 \pm 2.5$ | 7.96–8.86; 11.33–11.79 |
| 7 | $1027.3 \pm 5.2$ | $38.1 \pm 8.7$ | (6.71–7.46); 9.54–9.93 |
| 8 | $1161.7 \pm 2.5$ | $99 \pm 21$ | (6.31–7.02); 8.97–9.34 |
| 9 | $1831 \pm 13$ | $121 \pm 44$ | (5.02–5.59); 7.15–7.44 |
| 10 | $1973 \pm 10$ | $151 \pm 52$ | (4.84–5.38); 6.89–7.16 |
| 11 | $2129 \pm 5$ | $135 \pm 14$ | (4.66–5.18); 6.63–6.90 |
| 12 | $2599 \pm 5$ | $164 \pm 18$ | (4.22–4.69); 6.00–6.24 |
| 13 | $3075.5 \pm 7.4$ | $309 \pm 28$ | (3.88–4.31); 5.52–5.74 |
| 14 | $3616.5 \pm 2.8$ | $308 \pm 9$ | (3.58–3.98); 5.09–5.29 |
| 15 | $4526.3 \pm 7.5$ | $494 \pm 28$ | (3.20–3.55); 4.55–4.73 |
| 16 | $7374 \pm 62$ | $1410 \pm 225$ | (2.50–2.79); 3.56–3.71 |
| 17 | $9465 \pm 32$ | $1584 \pm 108$ | (2.21–2.46); 3.14–3.27 |
| 18 | $13765 \pm 53$ | $2608 \pm 196$ | (1.83–2.04); 2.61–2.71 |
| 19 | $18592 \pm 128$ | $4712 \pm 442$ | (1.58–1.75); 2.24–2.33 |

**Note.** Distances and widths from MOS2 (Obs1) for rings 0–4 and 7–8, from MOS2 (Obs2) for rings 5–6, from PN (Obs2) for rings 9–19. The minimum ($\theta_1$) and maximum ($\theta_2$) radii expected during each exposure are indicated in parentheses if no EPIC camera could fully image the ring and so its spectrum was not considered in the spectral fitting.

between the angles $\theta_1$ and $\theta_2$. The latter can be computed using the model by Draine (2003), which is based on an analytical approximation of the cross section for a mixture of spherical carbonaceous and silicate grains with the size distribution described in Weingartner & Draine (2001). This approach was used in the analysis of the X-ray rings produced by other GRBs (e.g., Tiengo & Mereghetti 2006), as well as for the Imaging X-ray Polarimetry Explorer (IXPE) observations of GRB 221009A (Negro et al. 2023). However, the approximation may be not accurate enough for our high-quality data, especially at the lowest energies (see, e.g., Figure 9 in Draine 2003).

Therefore, we implemented a more appropriate model, dubbed ringscat, based on the exact Mie calculation of the scattering cross section on spherical grains, adopting several grain compositions and size distributions (Mathis et al. 1977; Zubko et al. 2004). This was done as described in Appendix B, computing the scattering cross sections as for the xscat model (Smith et al. 2006) already available within the XSPEC spectral fitting package (Arnaud 1996). Based on Equation (4), we fit the spectra of each ring with the XSPEC model: constant * TBabs * zTBabs * ringscat * pegpwrlw, where ringscat accounts for the optical depth for different dust models $\Delta N_H \sigma_{\theta_{1,2}}(E)$; the constant is the inverse of the exposure time ($T_{exp}^{-1}$); and the prompt GRB spectrum, $f(E)$, is modeled as a power law (pegpwrlw) modified by absorption (Wilms et al. 2000) both in our Galaxy (TBabs) and in the host galaxy (zTBabs, with redshift fixed at $z = 0.151$; Malesani et al. 2023).

The ring produced by dust at 0.73 kpc (ring 6) is the brightest one observed in both observations and the only one for which we have a reasonable estimate of the quantity of dust

producing it. In fact, from the Lallement et al. (2022) 3D extinction map, we can assume $\Delta N_H = 8 \times 10^{20}$ cm$^{-2}$ (Appendix C). We first fit the spectra of ring 6 obtained in Obs2, when it had a radius of 11′.5. This large size reduces the impact of small-scale fluctuations in the dust spatial distribution, which cannot be tracked by the low spatial resolution map of Lallement et al. (2022). We fixed the Galactic absorption at $N_{H,G} = 7 \times 10^{21}$ cm$^{-2}$, which is the average value of the Planck Collaboration (2014) 2D map at the ring position.[17] By simultaneously fitting the PN and MOS2 spectra of Obs2,[18] we found that all the dust models gave statistically acceptable fits (see an example in the top panel of Figure 3) and yielded similar GRB spectral parameters, with values of the 0.5–5 keV fluence in the range $(2–4.5) \times 10^{-3}$ erg cm$^{-2}$ (see Table 2).

To discriminate between the different dust models and better constrain the spectral shape of the GRB prompt emission, we performed a similar analysis by simultaneously fitting the spectra of the other rings. The rings completely inside the MOS2 field of view in Obs1 (rings 1–6) are produced by dust in the range 350–800 pc, where a large extinction increase is clearly detected in 3D maps (Appendix C). Therefore, based either on Lallement et al. (2022) or Green et al. (2019), we can assume $\Delta N_H = 4 \times 10^{21}$ cm$^{-2}$ or $\Delta N_H = 2.3 \times 10^{21}$ cm$^{-2}$, respectively. The fluences derived using the former value are listed in Table 2 (obviously, the smaller value of $\Delta N_H$ would give ∼70% larger fluences), and the fit with the BARE-GR-B model is shown in the middle panel of Figure 3.

Finally, we performed a joint fit of the spectra of rings 1–19 (in addition to the MOS2 spectra, we included also the PN spectra of rings 7–19 during Obs2). According to the Akaike information criterion (Akaike 1974), the BARE-GR-B model (bottom panel of Figure 3) is strongly favored with respect to all the other dust models that we have considered.[19] The results reported in Table 2 were obtained assuming $\Delta N_H = 6.7 \times 10^{21}$ cm$^{-2}$ for the cumulative column density in the 19 dust clouds, based on Lallement et al. (2022). Over this broader distance interval, ranging from 350 pc to the edge of the Galaxy, the discrepancies between the Lallement et al. (2022) and Green et al. (2019) maps are smaller, giving only a 15% larger fluence if the total extinction is derived from the latter map.

### 3.3. Properties of the GRB Prompt Emission

We consider BARE-GR-B (Zubko et al. 2004) as our main reference model not only because it provides the best joint fit to the spectra of all the 19 X-ray rings but also because it resulted as the best-fitting model in previous studies of dust-scattering

---

[17] This value was assumed also in all the joint spectral fits of multiple rings only for ring 6, while the Galactic absorption for the other rings was let free to vary. We have verified that the resulting best-fit values for each ring are compatible with the $N_H$ radial profile derived from Planck Collaboration (2014). We note that the statistical uncertainties of most bins in such a radial profile is larger than that of the $N_{H,G}$ derived from the spectral fitting of the brightest X-ray rings.

[18] The MOS2 spectrum of Obs1 gave consistent results, except for a ∼15% lower GRB fluence, which can be explained by the fact that dust is not uniformly distributed in this sky area.

[19] Since we are comparing models with the same number of free parameters, applied to the same spectra, if we use the $\chi^2$ to represent the negative of twice the logarithm of the likelihood of the model, the difference between the Akaike information criterion (in the form valid for small sample sizes) of the two models is simply the difference between their $\chi^2$ values. We can therefore prefer the BARE-GR-B model because it has the lowest $\chi^2$ for the simultaneous fit to the 19 spectra, and the difference with all the other models is greater than 10, which is considered a reasonable threshold to reject a model (e.g., Burnham & Anderson 2002).
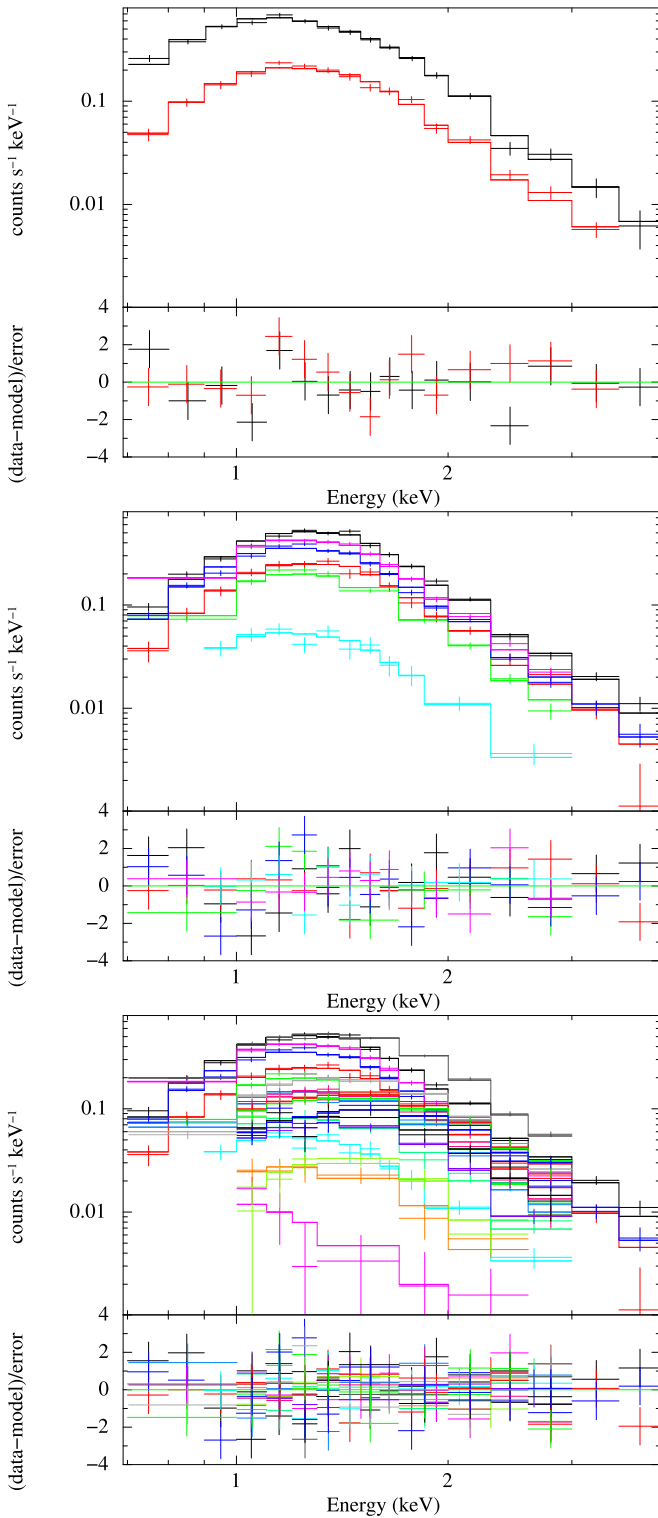
**Figure 4.** Map of the total hydrogen column density in the sky area around GRB 221009A (Planck Collaboration 2014; see Appendix C for details). The white circles (radii of 2′ and 12′) indicate the region covered by the X-ray rings during XMM-Newton observations.

**Figure 3.** Fit of the ring spectra with the BARE-GR-B model (best-fit parameters in Table 2). Top panel: PN (black) and MOS2 (red) spectra of ring 6 in Obs2. Middle panel: MOS2 spectra of rings 1–6 in Obs1. Bottom panel: MOS2 spectra of rings 1–6 in Obs1 and PN spectra of rings 7–19 in Obs2.

X-ray halos (e.g., Smith et al. 2006; Tiengo et al. 2010). However, to evaluate the impact of different choices of dust models on the spectral parameters of the prompt GRB emission, we consider also the COMP-GR-B, BARE-GR-S, and the Draine (2003) models, which give a reasonably good fit to the full set of spectra (Table 2). According to these models,
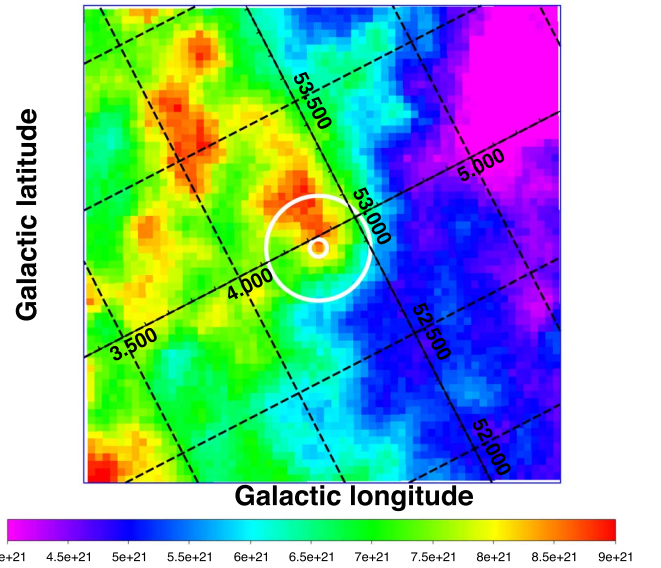
the power-law photon index of the GRB prompt emission ranges from $\sim$1.0 to $\sim$1.4, with the steepest slope ($1.37 \pm 0.04$) obtained with BARE-GR-B.

If we exclude the Draine (2003) model, which is not accurate enough at low energies, the hydrogen column density in the host galaxy can be constrained within the narrow range $N_{H,z} = (4.1\text{–}5.3) \times 10^{21}$ cm$^{-2}$ (Table 2). However, this result depends on the value of the absorption in our own Galaxy, which we fixed to $N_{H,G} = 7 \times 10^{21}$ cm$^{-2}$ for ring 6. To evaluate the impact of a different assumption on the Galactic absorption, we fixed it at $N_{H,G} = 5.38 \times 10^{21}$ cm$^{-2}$ (Willingale et al. 2013), obtaining for the BARE-GR-B model a slightly worse fit ($\chi^2$ from 194.34 to 200.08 for 155 degrees of freedom, d.o.f.) and an increase of $N_{H,z}$ from $(4.4 \pm 0.3) \times 10^{21}$ cm$^{-2}$ to $(6.6 \pm 0.4) \times 10^{21}$ cm$^{-2}$. Assuming instead $N_{H,G} = 9 \times 10^{21}$ cm$^{-2}$, which is the largest value displayed by the Planck Collaboration (2014) map within the region covered by the X-ray rings (Figure 4), we obtain a marginally better fit ($\chi^2 = 188.55$ for 155 d.o.f.) and an intrinsic absorption of $N_{H,z} = (1.8 \pm 0.2) \times 10^{21}$ cm$^{-2}$.

Our estimate of the GRB fluence depends on our assumptions on the column density of dust in the clouds, based on 3D extinction maps (Appendix C). First of all, we note that the fluence values for each dust model are systematically lower when a larger number of rings is considered (Table 2). This effect can be explained by the fact that the extinction excess derived from the maps includes also the contribution from diffuse (i.e., dust not concentrated in the layers associated to the rings) dust or unresolved scattering rings and should therefore be considered as an upper limit to the amount of dust in the thin layers generating the X-ray rings. The most conservative lower limit to the GRB fluence can therefore be derived from the fit of the spectra of the 19 rings with the Draine (2003) model,[20] which gives a GRB fluence of $1.25 \times 10^{-3}$ erg cm$^{-2}$.

---

[20] The same fluence is obtained also with the Mathis–Rumpl–Nordsieck (MRN) model (Mathis et al. 1977), which, however provides a very poor fit to the 19 spectra (null-hypothesis probability of $10^{-11}$).

**Table 2**
Best-fit Parameters of the GRB Prompt Emission Derived from Different Choices of Dust-scattering Rings and Dust Models

| Data set | Dust Model | $N_{\mathrm{H,z}}$[a] $(10^{21}\,\mathrm{cm}^{-2})$ | $\Gamma_{\mathrm{GRB}}$[b] | GRB Fluence[c] $(10^{-3}\,\mathrm{erg}\,\mathrm{cm}^{-2})$ | $\chi^2$/d.o.f. |
|---|---|---|---|---|---|
| Ring 6[d] | BARE-GR-B | $4.9 \pm 0.6$ | $1.3 \pm 0.1$ | $2.57 \pm 0.05$ | 36.77/30 |
| | BARE-GR-S | $5.0 \pm 0.6$ | $1.2 \pm 0.1$ | $2.52 \pm 0.05$ | 40.76/30 |
| | BARE-GR-FG | $5.0 \pm 0.6$ | $1.2 \pm 0.1$ | $2.52 \pm 0.05$ | 39.77/30 |
| | COMP-GR-B | $5.8 \pm 0.6$ | $1.2 \pm 0.1$ | $4.2 \pm 0.1$ | 45.55/30 |
| | COMP-GR-S | $5.3 \pm 0.5$ | $1.05 \pm 0.09$ | $4.4 \pm 0.1$ | 34.57/30 |
| | COMP-GR-FG | $5.9 \pm 0.6$ | $1.1 \pm 0.1$ | $4.0 \pm 0.1$ | 41.05/30 |
| | MRN | $6.7 \pm 0.6$ | $1.5 \pm 0.1$ | $2.03 \pm 0.04$ | 44.57/30 |
| | Draine (2003) | $6.7 \pm 0.5$ | $1.1 \pm 0.1$ | $2.41 \pm 0.06$ | 34.94/30 |
| Rings 1–6[e] | BARE-GR-B | $4.6 \pm 0.4$ | $1.39 \pm 0.05$ | $1.94 \pm 0.02$ | 103.83/72 |
| | BARE-GR-S | $5.3 \pm 0.4$ | $1.31 \pm 0.05$ | $1.87 \pm 0.02$ | 107.46/72 |
| | BARE-GR-FG | $5.6 \pm 0.4$ | $1.32 \pm 0.05$ | $1.89 \pm 0.02$ | 117.45/72 |
| | COMP-GR-B | $5.6 \pm 0.4$ | $1.17 \pm 0.05$ | $3.09 \pm 0.03$ | 110.10/72 |
| | COMP-GR-S | $6.7 \pm 0.4$ | $1.08 \pm 0.05$ | $3.23 \pm 0.04$ | 143.07/72 |
| | COMP-GR-FG | $6.3 \pm 0.5$ | $1.09 \pm 0.05$ | $2.91 \pm 0.04$ | 124.39/72 |
| | MRN | $7.5 \pm 0.5$ | $1.44 \pm 0.05$ | $1.55 \pm 0.02$ | 141.06/72 |
| | Draine (2003) | $7.1 \pm 0.4$ | $1.12 \pm 0.05$ | $1.59 \pm 0.02$ | 99.39/72 |
| Rings 1–19[f] | BARE-GR-B | $4.4 \pm 0.3$ | $1.37 \pm 0.04$ | $1.67 \pm 0.02$ | 194.34/155 |
| | BARE-GR-S | $4.6 \pm 0.4$ | $1.20 \pm 0.04$ | $1.53 \pm 0.01$ | 210.77/155 |
| | BARE-GR-FG | $4.6 \pm 0.3$ | $1.18 \pm 0.04$ | $1.54 \pm 0.01$ | 235.18/155 |
| | COMP-GR-B | $5.1 \pm 0.2$ | $1.08 \pm 0.04$ | $2.47 \pm 0.03$ | 204.99/155 |
| | COMP-GR-S | $5.2 \pm 0.2$ | $0.86 \pm 0.04$ | $2.52 \pm 0.03$ | 298.95/155 |
| | COMP-GR-FG | $5.0 \pm 0.4$ | $0.89 \pm 0.04$ | $2.28 \pm 0.02$ | 257.26/155 |
| | MRN | $6.0 \pm 0.4$ | $1.21 \pm 0.04$ | $1.24 \pm 0.01$ | 302.54/155 |
| | Draine (2003) | $6.3 \pm 0.4$ | $1.00 \pm 0.04$ | $1.25 \pm 0.01$ | 211.10/155 |

**Notes.** The Galactic absorption of ring 6 is fixed at $N_{\mathrm{H,G}} = 7 \times 10^{21}\,\mathrm{cm}^{-2}$. All uncertainties are at $1\,\sigma$.
[a] Absorption in the host galaxy ($z = 0.151$).
[b] Photon index of the GRB prompt emission.
[c] Unabsorbed GRB fluence in the 0.5–5 keV energy band.
[d] PN and MOS2 spectra of ring 6 in Obs2, assuming $\Delta N_{\mathrm{H}} = 8 \times 10^{20}\,\mathrm{cm}^{-2}$ in the dust cloud.
[e] MOS2 spectra of rings 1–6 in Obs1, assuming $\Delta N_{\mathrm{H}} = 4 \times 10^{21}\,\mathrm{cm}^{-2}$ in the six dust clouds.
[f] MOS2 spectra of rings 1–6 in Obs1 and PN spectra of rings 7–19 in Obs2, assuming $\Delta N_{\mathrm{H}} = 6.7 \times 10^{21}\,\mathrm{cm}^{-2}$ in the 19 dust clouds.

Excluding the COMP-GR-S model, which does not adequately fit the ring spectra, the largest fluence is derived adopting the COMP-GR-B model. Further increasing the value reported in Table 2 by assuming the extinction in the six dust clouds from (Green et al. 2019) and by considering that ∼30% of the dust between 350 and 800 pc might not be inside the six clouds, we set $7 \times 10^{-3}$ erg cm$^{-2}$ as the most conservative upper limit to the 0.5–5 keV fluence of GRB 221009A.

Our most reliable estimate for the GRB fluence is $2.6 \times 10^{-3}$ erg cm$^{-2}$, which is obtained by fitting the spectrum of ring 6 (not affected by the uncertain fraction of diffuse dust) with the BARE-GR-B model (i.e., our preferred dust model). However, also this value is affected by unavoidable systematic uncertainties, which, although difficult to quantify, are likely within the lower and upper limits derived earlier in this section. First of all, it is based on an excess of optical extinction detected (at the correct distance of 0.73 kpc) in a map with poor angular resolution (Lallement et al. 2022), while X-ray data exhibit clear evidence for small scale variations of the dust distribution in this cloud (Figure 5). Moreover, XMM-Newton can resolve two rings (ring 5 and 6) within the peak in the Lallement et al. (2022) map, but their relative intensity (ring 5 is about 3 times fainter than ring 6) is significantly different in the two observations. Since this indicates that these two dust clouds might have substantially different shapes and sizes, we attributed the whole extinction excess to the dust producing the brightest ring (ring 6). Finally, our fluence estimates depend on the conversion from $\Delta A_V$ to $\Delta N_{\mathrm{H}}$, which we have derived for our sky area from Planck Collaboration (2014) and Schlafly & Finkbeiner (2011; Appendix C). This relation is also affected by nonnegligible systematic uncertainties, as demonstrated by the scatter displayed by the measures reported in previous studies, covering different sky directions and astrophysical objects (e.g., Zhu et al. 2017).

## 4. Discussion

The large collecting area and wide field of view of XMM-Newton allowed us to detect 20 dust-scattering rings around the extremely bright GRB 221009A. They were produced by dust concentrations at distances between 300 pc and 18.6 kpc. Besides deriving accurate measurements of the distance of the dust layers from the time delay and position of the scattered photons (relative precision ranging from 0.05% to 0.8%; Table 1), we could constrain the prompt X-ray emission of the burst through a detailed spectral analysis.

Analysis of the GRB 221009A dust-scattering rings were also reported by Vasilopoulos et al. (2023) and Williams et al. (2023), who used Swift/XRT, and by Negro et al. (2023), who used IXPE data. Swift/XRT could already image the X-ray rings about 1 day after the GRB, making possible the discovery of dust clouds at distances smaller than 300 pc (Vasilopoulos et al. 2023), which formed X-ray rings that were already
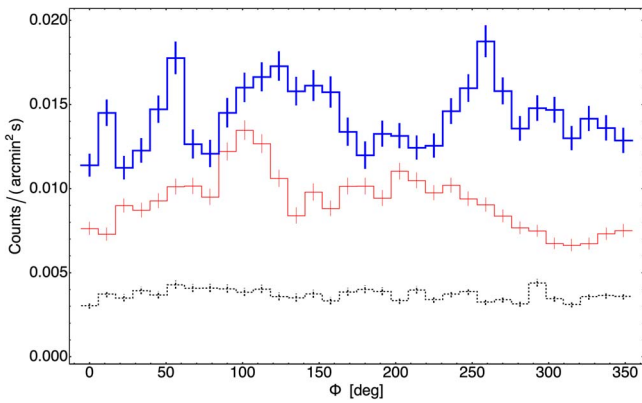
**Figure 5.** Azimuthal distribution of the MOS2 exposure-corrected surface brightness in the 0.7–4 keV band detected between $4\rlap{.}'8$ and $5\rlap{.}'8$ (thick solid blue line) and between $11\rlap{.}'1$ and $12\rlap{.}'1$ (thin solid red line) from the GRB position in Obs2. Each annulus contains two rings: 13 and 14, produced by dust at $\sim$3.5 kpc, and rings 5 and 6, produced by dust at $\sim$0.7 kpc. Both annuli are compared to the same background signal (black dashed line), extracted from an $8'$ –$10\rlap{.}'5$ annulus, where only two very faint rings (7 and 8) have been detected. All point sources have been excluded.

outside the EPIC field of view during XMM-Newton observations. On the other hand, thanks to a superior counting statistics and a different data analysis technique, we could detect fainter X-ray rings and identify multiple dust layers in large dust concentrations that were not resolved in Vasilopoulos et al. (2023). In particular, we detected an X-ray ring formed by dust at a distance of 18.6 kpc,[21] which, given the Galactic latitude $b = 4°\!.3$, implies the presence of dust up to $\sim$1.5 kpc above the Galactic plane in a region where it is difficult to obtain information on the interstellar dust while studying the optical extinction.

In addition, our analysis does not rely on a single model for the dust grain size distribution and composition. The use of different dust models (Mathis et al. 1977; Draine 2003; Zubko et al. 2004) allowed us to exclude some of them, including the MRN model (Table 2), which adequately fit the Swift/XRT data (Williams et al. 2023), and to evaluate their effect on the reconstruction of the GRB soft X-ray prompt emission.

The dust models were implemented using the exact Mie computation for the scattering process for spherical dust grains (Appendix B), which is valid in the whole energy range where the X-ray rings are detected (0.7–4 keV). In fact, the vast majority of the rings' signal in XMM-Newton has been detected below 2 keV, where X-ray scattering models based on the Rayleigh–Gans approximation are inadequate for the analysis of our high quality spectra.

Our best estimate of the X-ray fluence of GRB 221009A in the 0.5–5 keV band ($2.6 \times 10^{-3}$ erg cm$^{-2}$) is about 1 order of magnitude larger than the value obtained by extrapolating to lower energies the model of the prompt emission observed above 20 keV by Konus-Wind (Frederiks et al. 2023) and

GECAM-C (An et al. 2023) during the GRB 221009A main event.[22] Considering also the other dust models producing reasonable fits to the ring spectra (Table 2) and different proxies for the quantity of dust producing them (Appendix C), our analysis constrains the 0.5–5 keV fluence of GRB 221009A between $10^{-3}$ and $7 \times 10^{-3}$ erg cm$^{-2}$ (corresponding to $2.4 \times 10^{-3}$ to $1.3 \times 10^{-2}$ erg cm$^{-2}$ in the 1–10 keV range). This fluence still implies a significant soft excess with respect to the extrapolation of the prompt emission of GRB 221009A observed at higher energies.

A 1–10 keV fluence of $(1.6–6.1) \times 10^{-4}$ erg cm$^{-2}$ was instead estimated from the analysis of the dust rings observed with IXPE, which allowed Negro et al. (2023) to derive limits on the X-ray polarization of GRB 221009A. During the IXPE observations, the rings produced by dust closer than 2 kpc were outside the field of view, and due to the limited angular resolution and collecting area, only two rings corresponding to broad dust distributions centered at 3.75 and 14.41 kpc could be identified. The GRB fluence was then reconstructed using the Draine (2003) model, assuming that all the optical extinction at distances greater than 3 kpc is due to two narrow dust layers at such distances (Negro et al. 2023). As demonstrated by the complex dust distribution unveiled by our analysis of the XMM-Newton data, this is an overestimate of the quantity of dust in these dust layers, leading to a lower estimate of the GRB fluence. Moreover, as already noted, the fluences derived from the Draine (2003) model are smaller than those obtained from the other dust models, and although appropriate above 2 keV, where IXPE operates, this model cannot be safely used to extrapolate the ring spectra at lower energies.

It is important to stress that, contrary to the case of the fluences, the spectral slopes we derived for the GRB prompt emission do not depend on the assumed quantity of dust producing the rings. They depend only on the shape of the scattering cross section, which, in turn, is related to the composition, shape, and size distribution of the grains. Considering only the dust models giving reasonable fits to the 19 complete rings detected by XMM-Newton, the power-law photon index spans from 1 to 1.4. The steepest spectrum ($\Gamma_{\mathrm{GRB}} = 1.37 \pm 0.04$) is derived from the best-fitting model (BARE-GR-B), whereas a harder slope ($\Gamma_{\mathrm{GRB}} \sim 0.8$, with significant variability during the GRB evolution) is observed at the lowest energies by hard X-ray detectors during the peak of the main event (An et al. 2023; Frederiks et al. 2023; Ripa et al. 2023). Together with the larger GRB fluence derived from our analysis of the X-ray rings, this suggests the presence of a soft excess in the prompt emission of GRB 221009A.

The broadening of the typical synchrotron spectrum responsible for the main spectral peak is predicted in the numerical simulations of the lepto-hadronic models for GRBs. For example, Rudolph et al. (2022) showed that a broad, flat spectrum due to the synchrotron emission of secondary pairs from $\gamma\gamma$ annihilation may affect the spectral slopes below the spectral peak and lead to a low-energy excess in the spectrum (see also Wang et al. 2018). The indication of a soft excess derived from our analysis is at odds with what derived in other GRBs for which prompt soft X-ray data are available

---

[21] Actually, Vasilopoulos et al. (2023) report an excess in the Swift/XRT radial profiles that might be produced by dust at even larger distances (23 and 38 kpc). However, due to the lack of coherent expansion and the limited angular resolution, they interpret it as the scattering of the afterglow X-ray emission by closer dust clouds. Some indication of dust up to $\sim$20 kpc in Swift/XRT data is also reported by Williams et al. (2023), but its column density could not be constrained due to the limited statistics and the uncertainties in the GRB fluence (Figure 2 of Williams et al. 2023). The presence of dust at such large distances is confirmed by the XMM-Newton observations performed more than 20 days after the GRB (B. Vaia et al. 2023, in preparation).

[22] An even lower 0.5–5 fluence of $5^{+10}_{-2} \times 10^{-5}$ erg cm$^{-2}$ is obtained by extrapolating the 80–800 keV fluence observed by *GRBAlpha*, assuming the spectrum is observed during the first 4 s of the main GRB peak (Ripa et al. 2023).

(Oganesyan et al. 2017, 2018). Indeed, our measured fluence and spectral slope exclude the existence of a marked flattening of the prompt emission spectrum of GRB 221009A below a few keV or tens of keV, unless it is balanced by an additional component in the soft energy range. Since the expansion of the rings constrains the emergence of such a component within 1000 s from the main GRB event (Appendix A), we cannot exclude the possibility that it might be associated to the soft flare observed ∼350 s later or to the earliest phases of the X-ray afterglow (e.g., An et al. 2023).

The possibility to fit the scattered emission with a physically motivated model also in the soft X-ray band made it possible to constrain the absorption in the host galaxy in the range $N_{\rm H,z} = (4.1–5.3) \times 10^{21}$ cm$^{-2}$ (to be extended by ∼50%, if the systematic uncertainty on Galactic absorption is taken into account). These values are consistent with the intrinsic absorption $N_{\rm H,z} = (1.4 \pm 0.4) \times 10^{22}$ cm$^{-2}$ derived from the spectral fit of the afterglow observed with Swift/XRT (Williams et al. 2023), especially if we consider that it was obtained by assuming $N_{\rm H,G} = 5.38 \times 10^{21}$ cm$^{-2}$ (Willingale et al. 2013), whereas a larger Galactic absorption ($N_{\rm H,G} \sim 9 \times 10^{21}$ cm$^{-2}$) at the afterglow position is indicated by the Planck Collaboration (2014) map (Figure 4). The brightness of the GRB 221009A X-ray afterglow makes it possible to study the evolution of the local absorption with time (S. Campana et al. 2023, in preparation), and therefore our constraints on the absorption of the prompt emission are fundamental to understanding how the interstellar medium of the host galaxy was affected by the propagation of the GRB radiation.

Further studies of these extraordinary X-ray rings, including a detailed analysis of both the radial and azimuthal spectral variability of individual rings, will allow us to characterize better the Galactic interstellar medium, reducing the systematic uncertainties affecting the reconstruction of the GRB 221009A soft X-ray spectrum and the absorption in the host Galaxy. Furthermore, a detailed modeling, including also the different quantity of dust encountered by X-rays as the rings expand, is necessary to estimate the contamination of the X-ray afterglow by dust-scattered X-rays—especially at early times, when the ring size was smaller and GRB 221009A was observed with operating modes without full imaging capabilities.

## Appendix A
## X-Ray Ring Expansion and Azimuthal Variability

The top panels of Figure 6 show the MOS2 images obtained by dividing the first XMM-Newton observation into three time intervals, each with ∼16 ks exposure. More individual X-ray rings can be identified with respect to Figure 1, where some of them were superimposed due to their expansion during the observation. Such expansion can be evaluated from the comparison with the reference red circles (8′ and 11′ radii). The same red circles are displayed also in the bottom panels, where the corresponding images for the second XMM-Newton observation are shown for MOS1, MOS2, and PN. In this observation, performed more than 3 days later, the bright ring that was close to the inner red circle in Obs1 (actually comprising ring 5 and 6), had moved beyond the outer reference circle. We have verified that the expansion rate of ring 6, whose radius can be precisely measured in time-resolved images of both XMM-Newton observations, is consistent with an origin within ∼1000 s from the main GRB event.

The rings detected at larger radii in Obs1 (rings 0–4) were already at least partly outside the field of view of all the EPIC cameras in Obs2. The corresponding MOS1 image shows how this instrument could observe complete rings only with its central CCD, which was not operated in 2D imaging mode in Obs1.

Partially imaged rings were not considered for the spectral analysis in order to reduce the bias in the reconstruction of the GRB fluence caused by the marked azimuthal variation observed in the ring intensity. As an example, Figure 5 shows the azimuthal distribution of the surface brightness of the brightest X-ray rings in Obs2. The presence of adjacent bins with statistically incompatible surface brightness indicates significant variations on spatial scales as small as 1′.
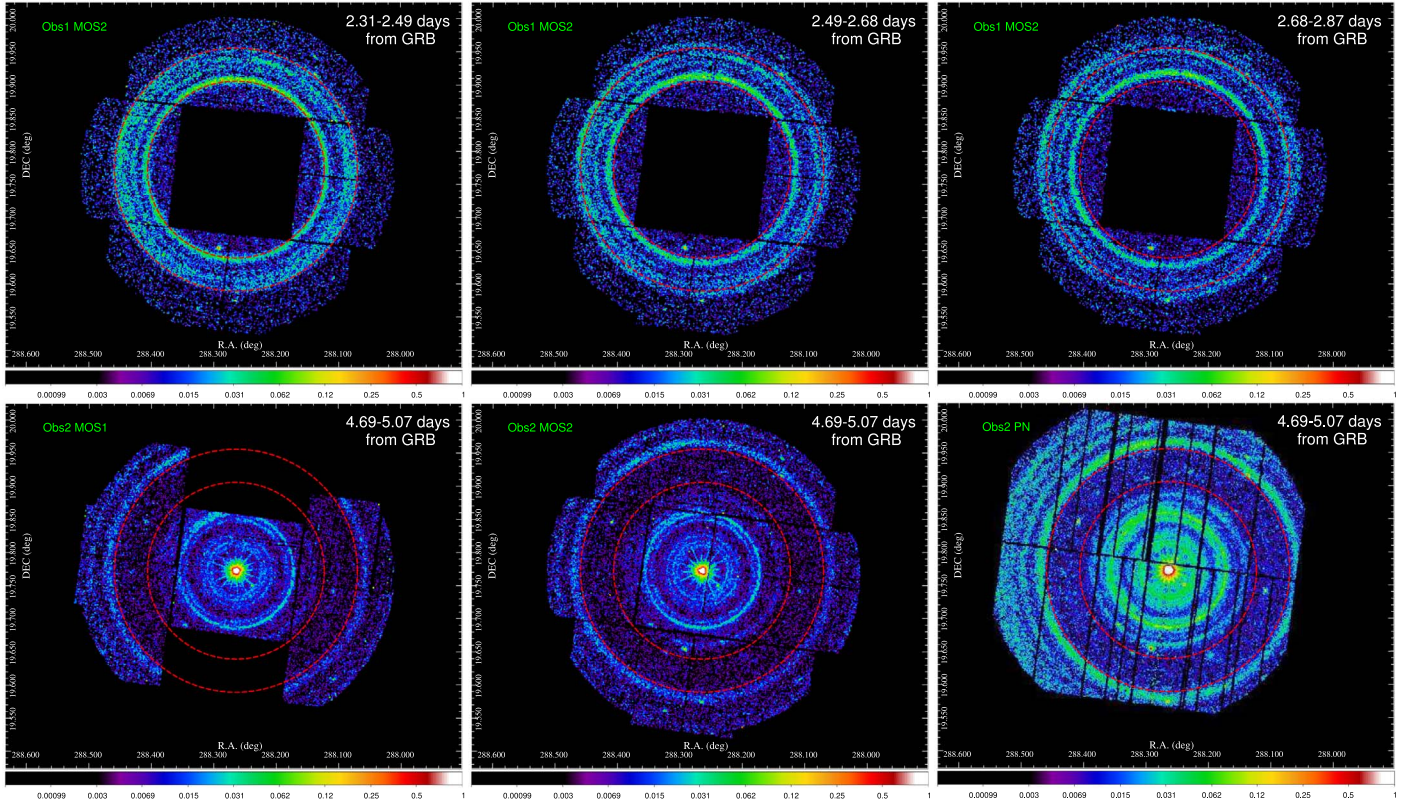
**Figure 6.** EPIC exposure-corrected 0.7–4 keV images, in units of counts s$^{-1}$ arcmin$^{-2}$, of the expanding rings from Obs1 (top panels: MOS2 data in three consecutive time intervals with ~16 ks of exposure time each) and Obs2 (bottom panels, from left to right: MOS1, MOS2, and PN data for the full 33 ks time interval of quiescent background). All the images have been smoothed with a Gaussian kernel of $\sigma = 2\rlap{.}''5$. Two red circles of radii $8'$ and $11'$ are shown as a reference for ring expansion.

## Appendix B
### The Dust-scattering Spectral Model

To reconstruct the GRB prompt emission from the spectrum of each ring (Equation (4)), we need a model for the optical depth, $\Delta N_{\mathrm{H}} \sigma_{\theta_{1,2}}(E)$, for single scattering between the angles corresponding to the inner ($\theta_1$) and outer ($\theta_2$) ring radius, for a population of dust grains with column density $\Delta N_{\mathrm{H}}$. We have therefore implemented a new XSPEC multiplicative model, called ringscat, whose input parameters are $\Delta N_{\mathrm{H}}$, $\theta_1$, $\theta_2$, and an integer number to identify different models for dust composition and grain size distribution.

To compute the scattering cross section, we took advantage of the publicly available software[23] developed to produce the XSPEC xscat model (Smith et al. 2016). This extinction model is based on the cross section for scattering at angles greater than $\theta$, $\sigma_\theta(E)$, computed using the exact Mie theory applied to a population of spherical grains. The cross section in ringscat can then be simply calculated as

$$\sigma_{\theta_{1,2}}(E) = \sigma_{\theta_1}(E) - \sigma_{\theta_2}(E). \tag{1}$$

In particular, we computed $\sigma_\theta(E)$ in the 0.4–4 keV energy range (with a resolution of 30 eV) for 38 angles between $2'$ and $12'$ for the following dust models: BARE-GR-B, BARE-GR-S, BARE-GR-FG, COMP-GR-B, COMP-GR-S, COMP-GR-FG (Zubko et al. 2004), and MRN (Mathis et al. 1977). The latter model assumes spherical grains with a power-law size distribution with index $-3.5$ between 0.005 and 0.25 $\mu$m.

The six models from Zubko et al. (2004), instead, combine different dust size distributions and compositions, including mostly bare graphite and silicate grains for the BARE-GR models, whereas composite particles containing silicates, organic refractory material, water ice, and voids are also considered in the COMP-GR models. The last part of the model names refers to the adoption of different abundances for the interstellar medium: solar (S), B-type (B), or F- and G-type (FG) stars.

## Appendix C
### Multiwavelength Constraints on the Galactic Interstellar Medium toward GRB 221009A

To derive the GRB fluence from the X-ray spectrum of a dust-scattering ring, we need an independent estimate of the quantity of dust in the corresponding dust cloud. Similarly, to constrain the amount of absorption in the host galaxy, we need to assume the value of the Galactic absorption in the direction of the X-ray rings. The latter information can be derived from 2D reddening maps (e.g., Schlafly & Finkbeiner 2011; Planck Collaboration 2014), whereas 3D maps (e.g., Green et al. 2019; Lallement et al. 2022) are required to evaluate the individual contribution of each dust cloud. The Lallement et al. (2022) map covers a $6 \times 6 \times 0.8$ kpc$^3$ volume with a resolution of 25 pc. The Green et al. (2019) data are instead defined on 120 distance bins logarithmically spaced in distances from 63 pc to 63 kpc, with angular sight lines of a typical scale ranging from $3\rlap{.}'4$ to $13\rlap{.}'7$.

The Lallement et al. (2022) 3D map in the GRB 221009A direction displays four prominent extinction peaks between 400

---
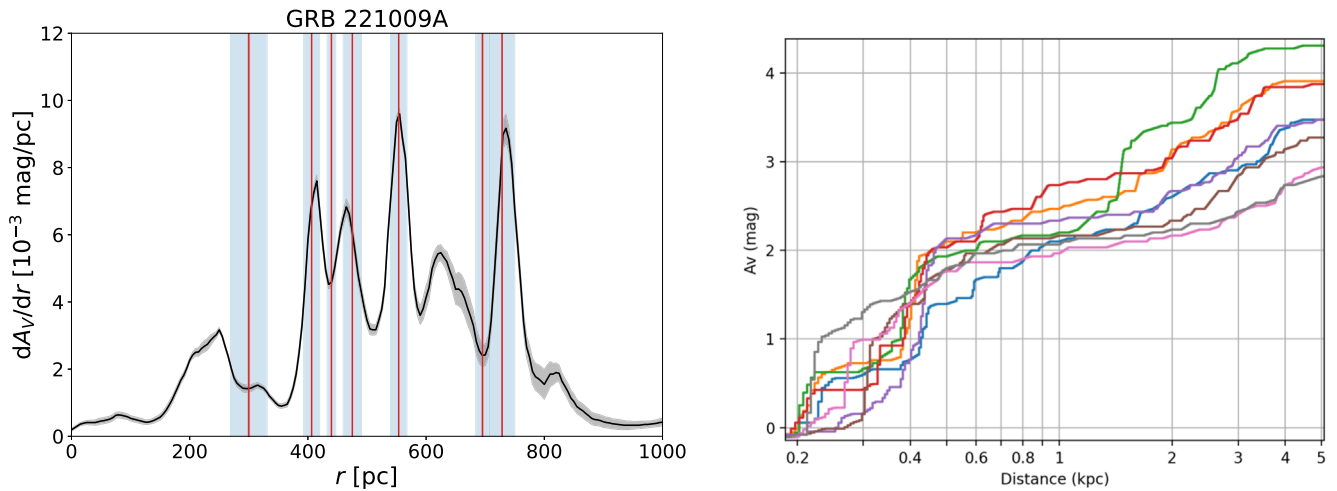[23] https://github.com/AtomDB/xscat

**Figure 7.** Left panel: differential extinction in the direction of GRB 221009A from Lallement et al. (2022), sampled every 5 pc and obtained using the G-Tomo app on the EXPLORE website (https://explore-platform.eu). Vertical red lines and light blue shaded areas indicate the distances and widths of dust layers producing rings 0–6 (Table 1). Right panel: cumulative extinction from Green et al. (2019) in eight equally spaced directions along the average position of ring 6 during Obs2 (∼11.5′ from GRB 221009A), extracted using the dustmaps software (Green 2018).

and 750 pc (left panel of Figure 7; B. Šiljeg et al. 2023, in preparation) at distances compatible with those derived from the brightest rings detected in Obs1 (rings 1, 3, 4, and 6; top panel of Figure 2). In particular, an extinction excess $\Delta A_V = 0.4$ mag can be associated with the dust that generated ring 6 (and possibly contributing also to ring 5), whereas the contribution from the other dust layers is more difficult to disentangle. The angular resolution of the Lallement et al. (2022) map at such distance (730 pc) is ∼2°, but the spatial variability of the ring intensity on arcminute scale (Figure 5) indicates that high-resolution maps would be required. However, the Green et al. (2019) map, which has better resolution, cannot detect significant extinction peaks that can be safely associated with individual X-ray rings (right panel of Figure 7).

A significant extinction excess $\Delta A_V = 1.2$ mag can instead be evaluated by selecting the voxels within 8′ and 12′ from GRB 221009A and at distances between 350 and 800 pc in the Green et al. (2019) map. The selected angular interval fully covers the six complete rings detected in Obs1 (rings 1–6), and the distance range includes all the dust layers producing them (Table 1). In the same distance interval, $\Delta A_V = 2.1$ mag is derived from Lallement et al. (2022).

Since the X-ray halo produced by dust closer than 350 pc was already outside the EPIC field of view during Obs1, the total amount of dust generating all the rings entirely observed by XMM-Newton can be derived from the difference between the total Galactic extinction reported in 2D maps and the optical extinction measured up to 350 pc in 3D maps. The extinction from 2D maps, derived from optically thin dust emission, should be preferred to the integration of 3D maps over the full distance range, which is known to underestimate the extinction at large distances, where the properties of background stars are difficult to constrain. Assuming $R_V = 3.1$, the average of the reddening values reported by Schlafly & Finkbeiner (2011) between 2′ and 12′ from GRB 221009A, where all the XMM-Newton rings were detected, translates into $A_V = 3.9$ mag. After the subtraction of the optical extinction within 350 pc, we estimate a residual extinction of 3.0 mag based on Green et al. (2019) and 3.5 mag according to Lallement et al. (2022).

In the same 2′–12′ annulus, assuming a conversion factor of $8 \times 10^{25}$ cm$^{-2}$ from dust optical depth at 353 GHz to hydrogen column density, obtained from the analysis of thermal dust emission with the Planck satellite (Planck Collaboration 2014), we derived an average Galactic $N_{H,G}$ toward GRB221009A of $7.4 \times 10^{21}$ cm$^{-2}$ (see Figure 4). This value, combined with the total optical extinction reported above, allows us to derive a conversion factor

$$N_H/A_V = 1.9 \times 10^{21} \, \text{cm}^{-2} \, \text{mag}^{-1}. \quad (2)$$

This factor is in the same range as the ratios obtained by averaging optical extinction and hydrogen column density derived from different samples of X-ray bright objects (e.g., Predehl & Schmitt 1995; Watson 2011; Zhu et al. 2017). This relation will be used in the spectral analysis to convert the extinction in the dust layers ($\Delta A_V$) into column density ($\Delta N_H$).

## ORCID iDs

Andrea Tiengo ● https://orcid.org/0000-0002-6038-1090
Fabio Pintore ● https://orcid.org/0000-0002-3869-2925
Beatrice Vaia ● https://orcid.org/0000-0003-0852-0257
Simone Filippi ● https://orcid.org/0000-0002-2119-9835
Andrea Sacchi ● https://orcid.org/0000-0002-7295-5661
Paolo Esposito ● https://orcid.org/0000-0003-4849-5092
Michela Rigoselli ● https://orcid.org/0000-0001-6641-5450
Sandro Mereghetti ● https://orcid.org/0000-0003-3259-7801
Ruben Salvaterra ● https://orcid.org/0000-0002-9393-8078
Barbara Šiljeg ● https://orcid.org/0000-0001-5391-8286
Andrea Bracco ● https://orcid.org/0000-0003-0932-3140
Željka Bošnjak ● https://orcid.org/0000-0001-6536-0320
Vibor Jelić ● https://orcid.org/0000-0002-6034-8610
Sergio Campana ● https://orcid.org/0000-0001-6278-1576

## References

Akaike, H. 1974, ITAC, 19, 716
An, Z.-H., Antier, S., Bi, X.-Z., et al. 2023, arXiv:2303.01203
Arnaud, K. A. 1996, in ASP Conf. Ser. 101, Astronomical Data Analysis Software and Systems V, ed. G. H. Jacoby & J. Barnes (San Francisco, CA: ASP), 17
Burnham, K. P., & Anderson, D. R. 2002, Information and Likelihood Theory: A Basis for Model Selection and Inference (New York: Springer), 49

Burns, E., Svinkin, D., Fenimore, E., et al. 2023, arXiv:2302.14037
Dichiara, S., Gropp, J. D., Kennea, J. A., et al. 2022, GCN, 32632, 1
Draine, B. T. 2003, ApJ, 598, 1026
Frederiks, D., Svinkin, D., Lysenko, A. L., et al. 2023, arXiv:2302.13383
Gabriel, C., Denby, M., Fyfe, D. J., et al. 2004, in ASP Conf. Ser. 314,
    Astronomical Data Analysis Software and Systems (ADASS) XIII, ed.
    F. Ochsenbein, M. G. Allen, & D. Egret (San Francisco, CA: ASP), 759
Green, G. 2018, JOSS, 3, 695
Green, G. M., Schlafly, E., Zucker, C., Speagle, J. S., & Finkbeiner, D. 2019,
    ApJ, 887, 93
Kennea, J. A., Williams, M. & Swift Team 2022, GCN, 32635, 1
Lallement, R., Vergely, J. L., Babusiaux, C., & Cox, N. L. J. 2022, A&A,
    661, A147
Malesani, D. B., Levan, A. J., Izzo, L., et al. 2023, arXiv:2302.07891
Mathis, J. S., Rumpl, W., & Nordsieck, K. H. 1977, ApJ, 217, 425
2014, Nasa High Energy Astrophysics Science Archive Research Center
    (Heasarc)HEAsoft: Unified Release of FTOOLS and XANADU,
    Astrophysics Source Code Library, ascl:1408.004
Negro, M., Di Lalla, N., Omodei, N., et al. 2023, 01798, arXiv:2301.01798
Oganesyan, G., Nava, L., Ghirlanda, G., & Celotti, A. 2017, ApJ, 846, 137
Oganesyan, G., Nava, L., Ghirlanda, G., & Celotti, A. 2018, A&A, 616, A138
Pintore, F., Tiengo, A., Mereghetti, S., et al. 2017, MNRAS, 472, 1465
Planck Collaboration 2014, A&A, 571, A11
Predehl, P., & Schmitt, J. H. M. M. 1995, A&A, 293, 889
Ripa, J., Takahashi, H., Fukazawa, Y., et al. 2023, arXiv:2302.10047
Rudolph, A., Petropoulou, M., Bošnjak, Ž., & Winter, W. 2022, arXiv:2212.00765
Schlafly, E. F., & Finkbeiner, D. P. 2011, ApJ, 737, 103
Smith, R. K., Dame, T. M., Costantini, E., & Predehl, P. 2006, ApJ, 648, 452
Smith, R. K., Valencic, L. A., & Corrales, L. 2016, ApJ, 818, 143
Strüder, L., Briel, U., Dennerl, K., et al. 2001, A&A, 365, L18
Tiengo, A., & Mereghetti, S. 2006, A&A, 449, 203
Tiengo, A., Pintore, F., Mereghetti, S., & Salvaterra, R. 2022, GCN, 32680, 1
Tiengo, A., Vianello, G., Esposito, P., et al. 2010, ApJ, 710, 227
Trümper, J., & Schönfelder, V. 1973, A&A, 25, 445
Turner, M. J. L., Abbey, A., Arnaud, M., et al. 2001, A&A, 365, L27
Vasilopoulos, G., Karavola, D., Stathopoulos, S. I., & Petropoulou, M. 2023,
    MNRAS, 521, 1590
Vaughan, S., Willingale, R., O'Brien, P. T., et al. 2004, ApJL, 603, L5
Vaughan, S., Willingale, R., Romano, P., et al. 2006, ApJ, 639, 323
Veres, P., Burns, E., Bissaldi, E., et al. 2022, GCN, 32636, 1
Vianello, G., Tiengo, A., & Mereghetti, S. 2007, A&A, 473, 423
Wang, K., Liu, R.-Y., Dai, Z.-G., & Asano, K. 2018, ApJ, 857, 24
Watson, D. 2011, A&A, 533, A16
Weingartner, J. C., & Draine, B. T. 2001, ApJ, 548, 296
Williams, M. A., Kennea, J. A., Dichiara, S., et al. 2023, arXiv:2302.03642
Willingale, R., Starling, R. L. C., Beardmore, A. P., Tanvir, N. R., &
    O'Brien, P. T. 2013, MNRAS, 431, 394
Wilms, J., Allen, A., & McCray, R. 2000, ApJ, 542, 914
Zhu, H., Tian, W., Li, A., & Zhang, M. 2017, MNRAS, 471, 3494
Zubko, V., Dwek, E., & Arendt, R. G. 2004, ApJS, 152, 211